JOURNAL OF MATERIALS SCIENCE 22 (1987) 689–700

Inclusion effects on submerged-arc weld microstructure

J. JANG, J. E. INDACOCHEA
Civil Engineering, Mechanics and Metallurgical Engineering Department, University of Illinois at Chicago, Chicago, Illinois 60680, USA

Bead-on-plate welds were produced using twenty four fused reagent grade submerged arc welding fluxes, selected from three flux systems, $SiO_2-MnO-FeO$, $SiO_2-MnO-CaF_2$ and $SiO_2-CaO-CaF_2$. The welds were processed using AISI 1010 steel coupons, and a Lincoln L-50 (AWS type A5.17) welding wire with a constant heat input of 3.0 kJ mm^{-1}. The three flux systems were selected because of their different oxygen potentials and their ability to produce welds with a wide oxygen range (70 to 1400 p.p.m.). Qualitative and quantitative metallography and chemical analysis were performed on the welds. Inclusion morphology and volume fraction are observed to be affected by flux composition. Inclusions of 1 μm in size and greater are associated with grain boundary and blocky proeutectoid ferrites, while inclusions 0.6 μm and smaller are linked with the presence of acicular ferrite.

1. Introduction

The detrimental effect of high oxygen contents on the toughness of submerged arc welds is well documented [1–6]. Oxygen can be introduced into the weld metal from several sources: the flux, the welding wire, the base metal and the atmosphere. The greatest oxygen contribution comes from the fluxes, since conventional submerged-arc welding of steel employs oxide-bearing fluxes. The oxygen-bearing electrode wire is the second greatest potential source of oxygen. The oxygen pick-up from the atmosphere is a minor contributor to the total weld oxygen content and it is just considered a contamination [7].

The concept of basicity was first introduced in the iron and steelmaking industry to describe the refining capability of slags. This concept has been further extended to characterize the flux behaviour in submerged-arc welding in terms of the oxygen transfer from the flux to the weld metal. Tuliani, *et al.* [8] proposed a popular basicity index (BI):

$$BI = \frac{\%CaO + \%CaF_2 + \%MgO + \%K_2O + \%Na_2O + 0.5(\%MnO + FeO)}{\%SiO_2 + 0.5(\%Al_2O_3 + \%TiO_2 + ZrO_2)}$$

It is well recognized that the higher the basicity index, the cleaner the weld with regard to non-metallic oxide inclusions. It has also been reported that fluxes with high basicity indexes reduce the weld metal oxygen levels and improve the toughness [1, 9, 10].

Taylor and Farrar, [11], working with submerged arc weld metals with oxygen contents in the range 300 to 1200 p.p.m. reported that oxygen levels greater than 600 p.p.m. corresponding to high concentrations of non-metallic inclusions, had a negative effect on both the Charpy upper shelf toughness and the ductile to brittle transition temperature. Similar results were obtained by Ito and Nakanishi [3], who observed that decreasing the weld oxygen levels improved greatly the impact properties, however, for a few cases when the oxygen content was below 200 p.p.m., there was deterioration in the toughness. They attributed this to an increase in hardenability of the weld metal due to increased silicon and manganese contents, which favoured the formation of lath-like or bainitic structures. Terashima and Tsuboi [12] found that oxygen levels above or below 300 p.p.m. led to a decrease in weld toughness, while Devillers and co-workers [13] in their work determined an optimum oxygen level between 400 and 500 p.p.m. for the ductile to brittle transition temperature.

The influence of oxygen on weld toughness has been closely correlated with the presence of non-metallic oxide inclusions in the weld metal. But the fact that reductions in the inclusion volume fraction below a critical value, would result in lower weld toughness, made investigators undertake detailed microstructural analysis with a view to correlating the changes in weld notch toughness with changes in microstructure.

Several microconstituents can be observed in ferritic weld metals, but confusion has existed in the terminology used to describe the different ferrite morphologies. Recently, a scheme for the identification of ferritic weld microstructures has been introduced [14]. There seems to be a general agreement that a microstructure primarily consisting of acicular ferrite will give the optimum weld metal mechanical properties, both strength and toughness, by virtue of its small grain size and high angle grain boundaries [5].

The presence of inclusions has been shown to affect qualitatively and quantitatively the final weld metal microstructure [5, 15–18]. Several models have been put forth to explain the effects of inclusions in the weld

0022–2461/87 $03.00 + .12

metal on the formation of acicular ferrite. Such models include lattice disregistry model, differential thermal strain model, inclusion type model, grain boundary pinning model and inclusion size distribution model.

The lattice disregistry model, as proposed by Bramfitt [19], takes into consideration the mismatch between the substrate and the nucleating phase as influencing the free energy of nucleation. The smaller the mismatch between the substrate (e.g. an inclusion) and the nucleating phase, the greater the tendency for nucleation of the new phase. While some have considered TiN to be the nucleating species [3], others think that oxide inclusions are responsible for the nucleation because of the low lattice disregistry between TiO and ferrite [20–22]. Although, others favoured the aluminum rich inclusions [23]. The strain energy involved in the phase transformation is also expected to affect the thermodynamic driving force of nucleation. It has been found that the thermal expansion coefficient of the austenitic iron matrix is much higher than that of the oxide inclusions [24, 25]. On cooling, because of the different thermal contraction between matrix and inclusion a strain energy is developed that will increase the thermodynamic driving force favouring the austenite to ferrite transformation.

The other proposed models that deal with the inclusion/acicular ferrite connection, focus on the composition and size of the inclusion and its interaction with the weld hardenability and the austenite grain boundary. The chemistry of the inclusion may influence the local weld chemical composition in the neighbourhood of the inclusion affecting the localized hardenability [5, 15, 26, 27], and thus influencing primarily the intragranular formation of a specific microconstituent. Inclusions located at the austenite grain boundaries affect also the austenite to ferrite transformation. Cochrane and Kirkwood [4] explained that coarser inclusions associated with high weld oxygen levels would pin the austenite grain boundary and serve as nucleation sites for Widmanstatten ferrite at the grain boundaries. Farrar *et al.* [17, 28] also suggested that the high volume fraction of oxide-rich inclusion in high oxygen welds tend to decrease the austenite grain size and increase the grain boundary areas favouring higher temperature grain boundary nucleated ferrite.

The arguments presented above reflect the significance of oxygen on the microstructural development and notch toughness of submerged arc welds. Contradictions still stand as to the specific mechanism by which oxygen, through the presence of non-metallic inclusions, influence the phase transformations in the weld metal. However, factors such as the chemical composition and weld thermal cycles, cannot be ignored. Furthermore, these factors are intimately connected with the models presented for the inclusion/weld microstructure [29].

In the present study, several bead-on-plate welds were made on an AISI-1010 steel plate by systematically varying the flux composition. Three flux systems were selected with one electrode filler wire. The weld inclusions were monitored in terms of their shape, size distribution and composition and correlated with the weld microstructure.

TABLE I Base metal and filler metal compositions

Material	Composition (wt %)						
	C	Mn	P	S	Si	Ti	Al
Base metal	0.07	1.41	0.038	0.015	0.53	0.076	0.055
Filler metal (L-50)	0.09	0.95	0.030	0.050	–	–	–

2. Experimental procedure

Several bead-on-plate welds were made on a 12.7 mm (0.50 in) thick AISI-1010 steel plate with a 3.18 mm (1/8 in) diameter filler metal electrode, Lincoln L-50 (AWS type A5.17). The base metal and welding wire compositions are reported in Table I. Three flux systems were selected for this study, SiO_2–MnO–FeO, SiO_2–MnO–CaF_2 and SiO_2–CaO–CaF_2, with systematic changes in composition made to cover the acid to basic ranges. Table II gives the flux matrix of the 24 different fluxes investigated. All these experimental fused fluxes were processed using reagent grade chemical powders.

The welds were automatically processed using a constant potential d.c. power supply controlled by a microprocessor. Constant welding conditions were used throughout, such that: voltage 28 V, current 550 A, travel speed 305 mm min^{-1} (12 i.p.m.), heat input 3.0 kJ mm^{-1} (77.8 kJ in^{-1}), d.c. reverse polarity. To eliminate inconsistencies, all the welds were made 140 mm (5.5 in) long, with samples extracted from the middle for metallographic evaluation and chemical analyses. Bulk weld chemistries were obtained with emission spectroscopy and inert gas fusion and are shown in Table III.

TABLE II Flux matrix composition (wt %) and basicity indeces

Sample number	SiO_2	FeO	MnO	CaO	CaF_2	*BI*
J2	40	5	55	0	0	0.75
J3	40	10	50	0	0	0.75
J4	40	15	45	0	0	0.75
J5	40	20	40	0	0	0.75
J6	40	0	60	0	0	0.75
J7	40	0	55	0	5	0.81
J8	40	0	50	0	10	0.88
J9	40	0	45	0	15	0.94
J10	40	0	40	0	20	1.00
J11	40	0	0	40	20	1.50
J12	40	0	0	35	25	1.50
J13	40	0	0	30	30	1.50
J14	40	0	0	25	35	1.50
J15	40	0	0	20	40	1.50
J16	30	0	0	50	20	2.33
J17	30	0	0	45	25	2.33
J18	30	0	0	40	30	2.33
J19	30	0	0	35	35	2.33
J20	30	0	0	30	40	2.33
J21	30	0	0	25	45	2.33
J22	20	0	0	60	20	4.00
J23	20	0	0	55	25	4.00
J24	20	0	0	50	30	4.00
J25	20	0	0	45	35	4.00

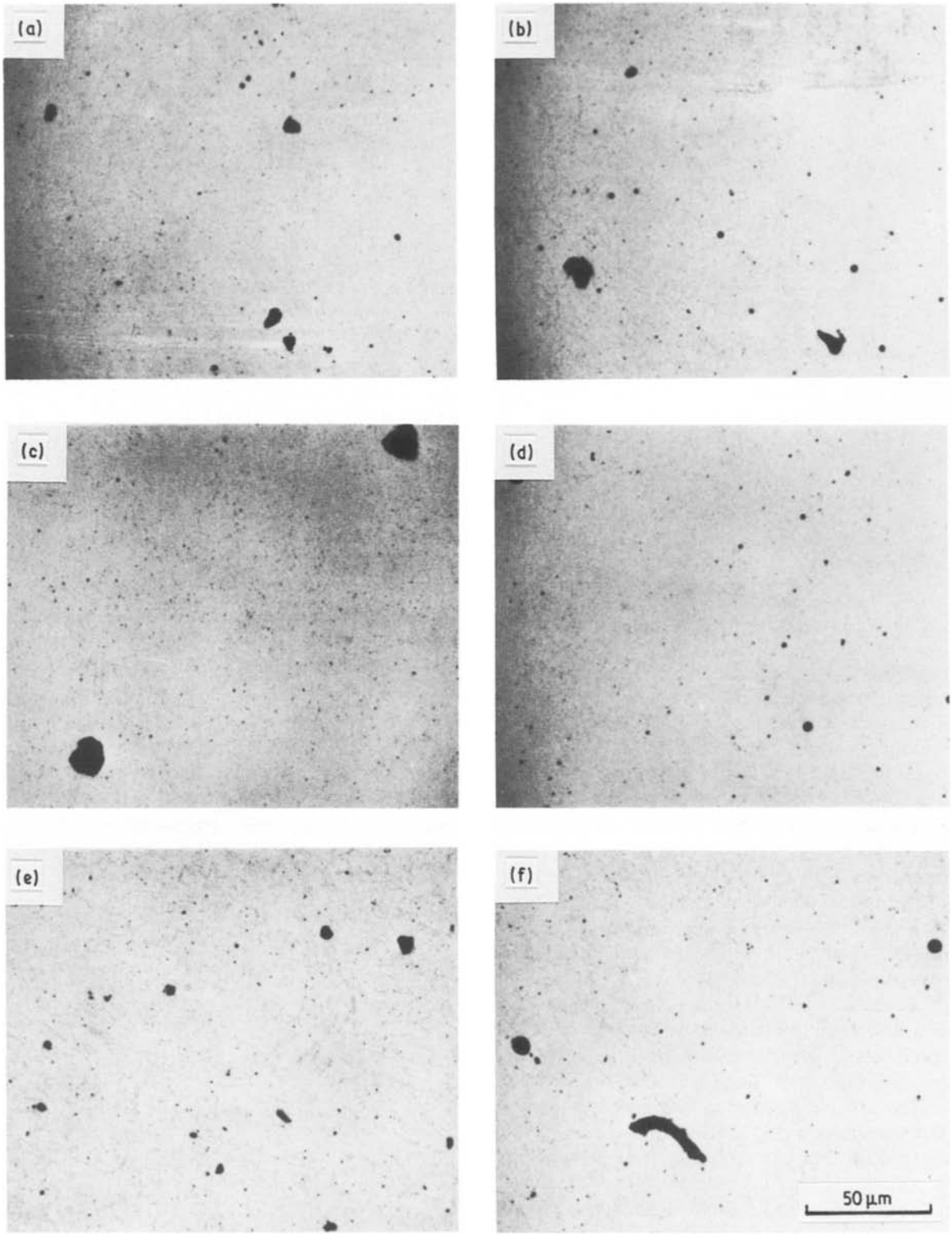

Figure 1 Weld inclusion morphologies found in this study for some fluxes. (a) $40SiO_2-50MnO-10FeO$, (b) $40SiO_2-40MnO-20FeO$, (c) $40SiO_2-60MnO$, (d) $40SiO_2-55MnO-5CaF_2$, (e) $40SiO_2-20CaO-40CaF_2$, (f) $40SiO_2-30CaO-30CaF_2$.

Characterization of the weld metal microstructure was carried out with light and scanning electron microscopes. Qualitative and quantitative metallography were conducted in assessing the ferrite morphologies. Scanning electron microscopic techniques were employed primarily to evaluate the composition and distribution of the inclusions in the weld metal.

3. Inclusion characterization

Weld samples were polished and examined under the light microscope to characterize the shape, size distribution and volume fraction of the inclusions.

Most of the non-metallic inclusions examined in all of the solid welds were spherical, but others showed triangular, irregular spheres and complex morphologies, as shown in Fig. 1. The inclusion shape was seen to be influenced by the flux composition as observed by other investigators [23, 30], however systematic variations within a specific flux system did not alter the inclusion shape. In the SiO_2-MnO based flux

TABLE III Chemical analysis of weld metal and base metal

Sample	Flux composition	C(%)	Mn(%)	P(%)	S(%)	Si(%)	Ti(%)	Al(%)	O(p.p.m.)
(J2)	$40SiO_2$–5FeO–55MnO	0.078	1.01	0.010	0.019	0.49	0.002	0.026	1209
(J3)	$40SiO_2$–10FeO–50MnO	0.082	1.00	0.010	0.021	0.54	0.002	0.050	1188
(J4)	$40SiO_2$–15FeO–45MnO	0.104	0.95	0.009	0.023	0.51	0.002	0.069	1188
(J5)	$40SiO_2$–20FeO–40MnO	0.081	0.85	0.009	0.021	0.48	0.002	0.056	1361
(J6)	$40SiO_2$–CaF_2–60MnO	0.093	0.96	0.010	0.020	0.38	0.002	0.043	1275
(J7)	$40SiO_2$–$5CaF_2$–55MnO	0.096	1.37	0.011	0.020	0.52	0.002	0.035	892
(J8)	$40SiO_2$–$10CaF_2$–50MnO	0.087	1.13	0.010	0.020	0.46	0.002	0.009	1019
(J9)	$40SiO_2$–$15CaF_2$–45MnO	0.082	0.93	0.010	0.020	0.38	0.002	0.039	941
(J10)	$40SiO_2$–$20CaF_2$–40MnO	0.079	0.93	0.011	0.019	0.43	0.002	0.031	823
(J11)	$40SiO_2$–40CaO–$20CaF_2$	0.099	0.50	0.009	0.021	0.42	0.002	0.018	451
(J12)	$40SiO_2$–35CaO–$25CaF_2$	0.101	0.49	0.010	0.021	0.39	0.002	0.009	456
(J13)	$40SiO_2$–30CaO–$30CaF_2$	0.102	0.49	0.010	0.021	0.40	0.002	0.007	564
(J14)	$40SiO_2$–25CaO–$35CaF_2$	0.098	0.45	0.011	0.021	0.44	0.002	0.008	529
(J15)	$40SiO_2$–20CaO–$40CaF_2$	0.097	0.46	0.011	0.022	0.43	0.002	0.007	457
(J16)	$30SiO_2$–50CaO–$20CaF_2$	0.105	0.63	0.010	0.016	0.27	0.002	0.008	237
(J17)	$30SiO_2$–45CaO–$25CaF_2$	0.106	0.61	0.010	0.017	0.28	0.002	0.008	249
(J18)	$30SiO_2$–40CaO–$30CaF_2$	0.104	0.59	0.009	0.019	0.32	0.002	0.008	303
(J19)	$30SiO_2$–35CaO–$35CaF_2$	0.106	0.56	0.010	0.019	0.32	0.002	0.008	307
(J20)	$30SiO_2$–30CaO–$40CaF_2$	0.101	0.52	0.010	0.019	0.35	0.002	0.008	362
(J21)	$30SiO_2$–25CaO–$45CaF_2$	0.103	0.52	0.010	0.020	0.36	0.002	0.008	357
(J22)	*$20SiO_2$–60CaO–$20CaF_2$	–	–	–	–	–	–	–	132
(J23)	*$20SiO_2$–55CaO–$25CaF_2$	–	–	–	–	–	–	–	109
(J24)	*$20SiO_2$–50CaO–$30CaF_2$	–	–	–	–	–	–	–	75
(J25)	*$20SiO_2$–45CaO–$35CaF_2$	–	–	–	–	–	–	–	164

*Poor welds, unable to perform all chemical analyses.

system, the inclusions present in welds produced with the eutectic flux were irregular spheres and non uniform triangles, but became predominantly spherical with additions of CaF_2 at the expense of MnO, while the introduction of FeO caused the inclusions to assume complex and irregular spherical shapes. Further increases of FeO or CaF_2 in the fluxes did not affect the already existing morphologies except the inclusion size.

The inclusions in the welds produced with the basic fluxes, SiO_2–CaO–CaF_2 flux system, were a homogeneous mixture of globular, irregular sphere and well defined triangular shapes. Variations in the basicity index between 1.5 and 4.0 for this flux system did not make a difference in the inclusion morphology. The same can be said when considering the basicity variation in the acid fluxes. From these results the morphology of the inclusions is seen to be more dependent on the flux constituents than on the flux basicity.

As expected, the weld oxygen level varied according to the stability of the oxide constituents of the fluxes. For example, in the SiO_2–MnO–FeO fluxes, because FeO and MnO are very unstable oxides, welds with very high oxygen levels were expected and these results are observed in Fig. 2. The welds produced with the SiO_2–MnO–CaF_2 fluxes show lower oxygen contents, Fig. 2, because CaF_2, a non-oxygen carrier, reduces the oxygen in the flux in replacing the MnO. Ca–O bonds are known to be much stronger than Si–O bonds [31], thus the degree of dissociation of calcium oxide in the molten flux would be less than that of silica, resulting in a lower weld metal oxygen content. Therefore, the reduction in the silica level of the fluxes and the increasing contents of CaO and CaF_2 produced welds with low oxygen contents as shown in Fig. 3. In terms of the basicity concept, as reported by other investigators [1, 9, 10], the correlation between flux basicity and weld metal oxygen content holds for the welds in this work, the substitution of SiO_2 by CaO and CaF_2 made the fluxes more basic and the corresponding welds had lower oxygen levels, as observed in Tables II and III.

Inclusion volume fraction measurements were performed on all the welds by taking readings at six different locations with a magnification of 1600 ×. The measurements were conducted according to the ASTM Standard E45. The weld inclusion content

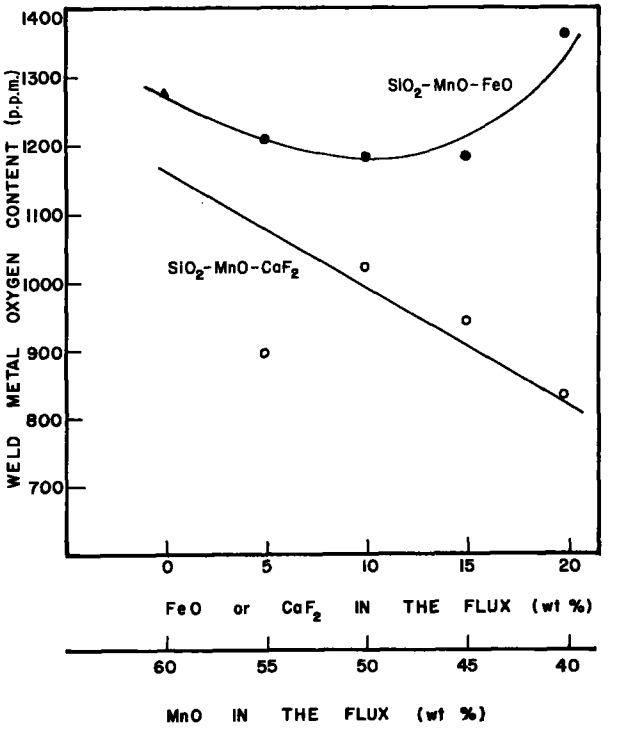

Figure 2 Weld metal oxygen content as function of FeO and CaF_2 addition to the SiO_2–MnO base flux. SiO_2 = 40% (constant), (▲) Eutectic flux.

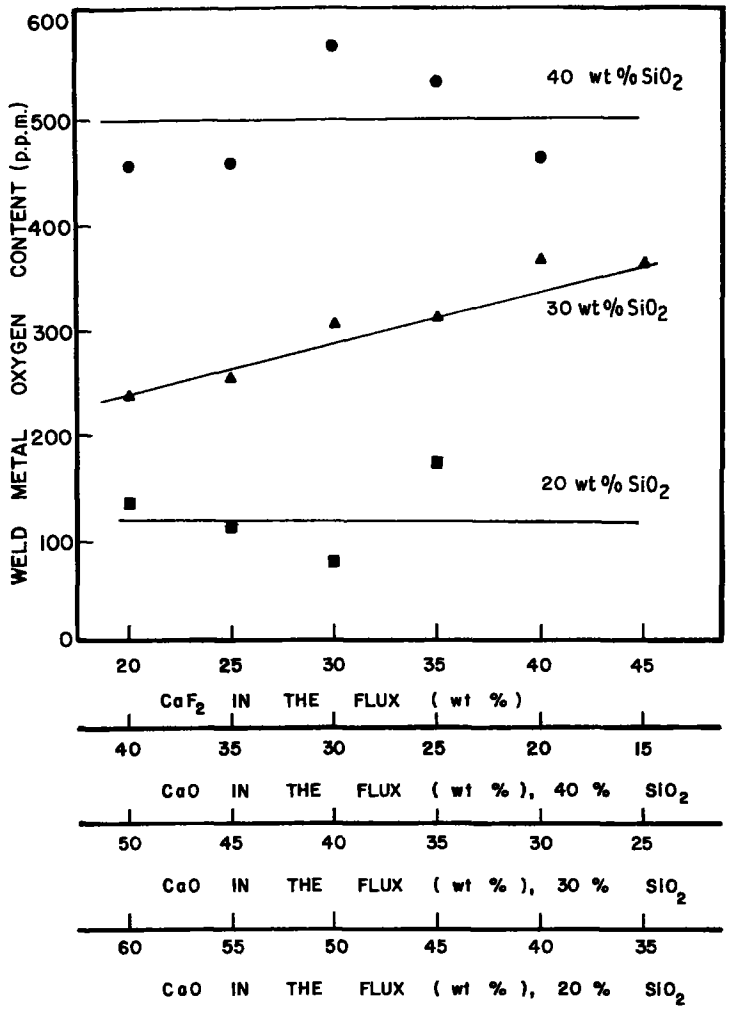

Figure 3 Weld metal oxygen content as function of CaF_2 and CaO contents in the SiO_2–CaO–CaF_2 flux system for fixed levels of SiO_2 at 40 30 and 20 wt %.

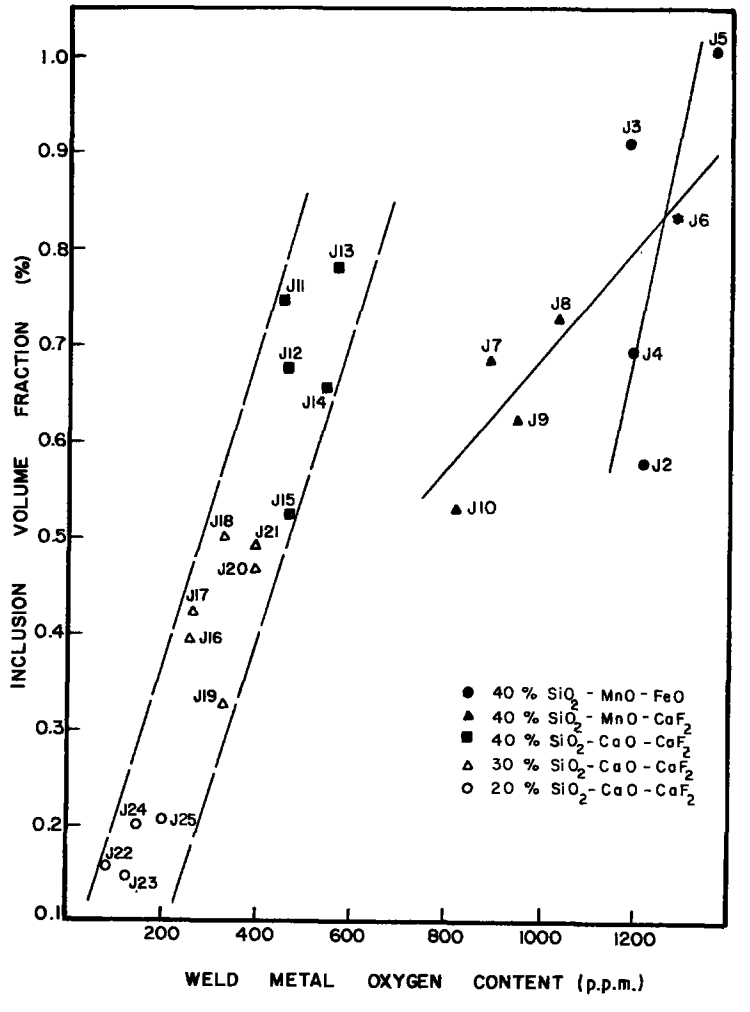

Figure 4 Inclusion volume fraction in the weld as a function of the weld metal oxygen content for all the weld specimens in this study.

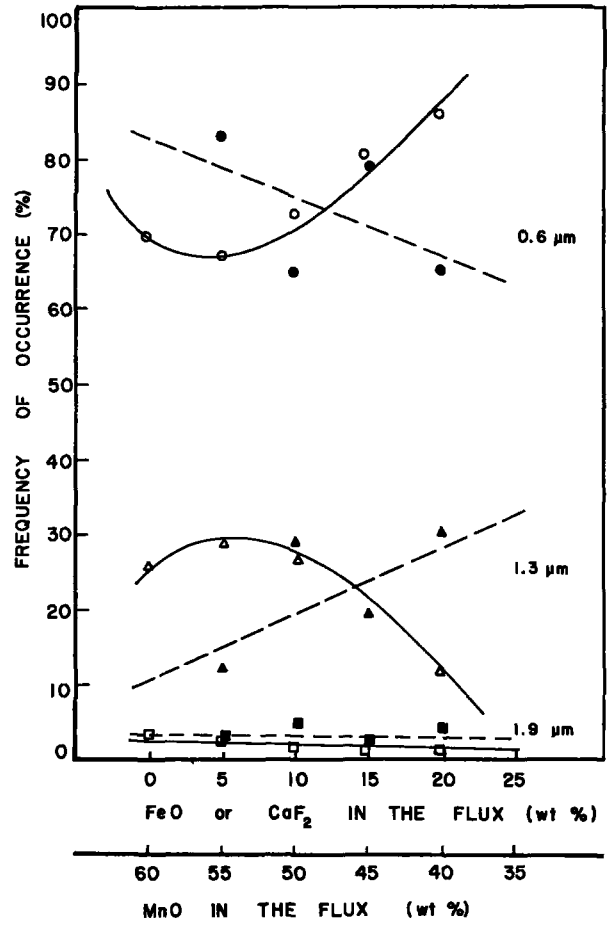

Figure 5 Inclusion size distribution for the welds produced with the (--- ● ▲ ■) SiO_2–MnO–FeO and (—— ○ △ □) SiO_2–MnO–CaF_2 fluxes. SiO_2 = 40% (constant).

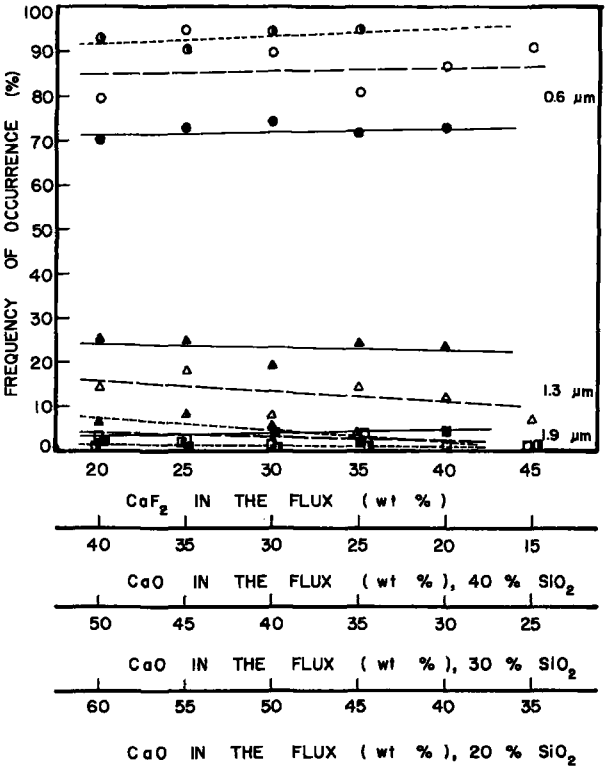

Figure 6 Inclusion size distribution for the welds produced with the SiO_2–CaO–CaF_2 fluxes. (—— ● ▲ ■) 40% SiO_2, (—— ○ △ □) 30% SiO_2, (---- ◑ ◭ ◨) 20% SiO_2.

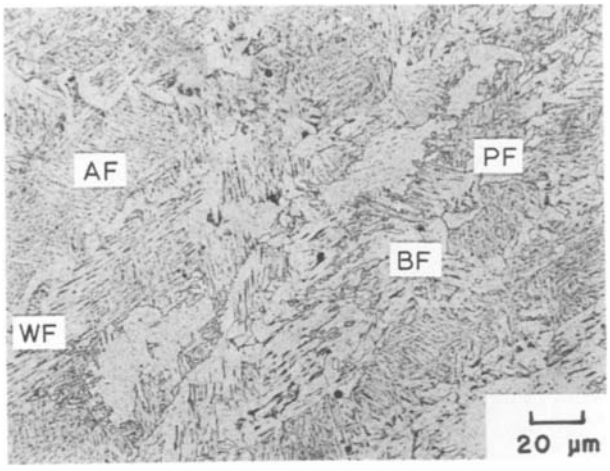

Figure 7 Typical ferrite morphologies encountered in this investigation. PF = proeutectoid grain boundary ferrite, AF = acicular ferrite, WF = Widmanstatten side plate ferrite, BF = blocky ferrite. 2% nital etch.

varies proportionally to the level of oxygen in the weld because of the oxide nature of the inclusions [4, 15], as shown in Fig. 4. The inclusion size also depends on the oxygen level of the welds, coarse inclusions are present in the high oxygen welds and they decrease in size as the level of oxygen is reduced, Figs 5 and 6.

4. Microstructural analysis

The principal weld microconstituents identified in this study are shown in Fig. 7: proeutectoid grain boundary ferrite (P F), acicular ferrite (A F), Widmanstatten side plate ferrite (W F), and intragranular blocky ferrite (B F). The quantitative metallography was limited to measurements of the acicular ferrite, Fig. 8, performed by the point count technique.

The acicular ferrite (A F) level, present in the welds, has been plotted against the inclusion volume fraction for all the flux systems studied, Fig. 9. These data show that the level of acicular ferrite cannot be just correlated with an optimum inclusion volume fraction. But other factors such as weld metal hardenability, cooling rate, etc., would play a role in the microstructure of the as-deposited ferritic weld metal [29, 32, 33]. Fig. 10 shows that the welds produced with the SiO_2–MnO–CaF_2 fluxes have larger

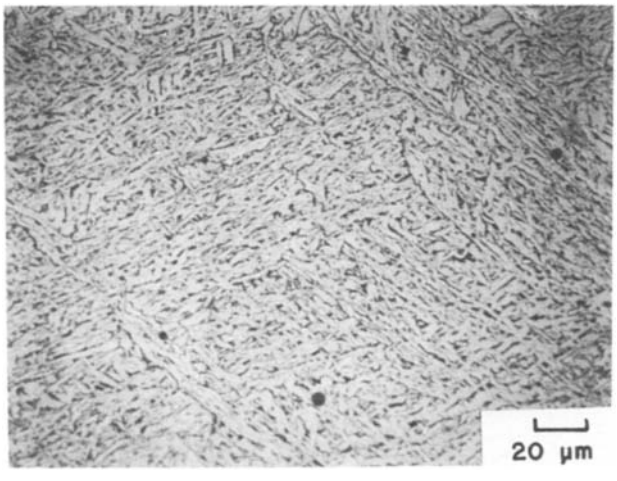

Figure 8 Fine grain acicular ferrite. 2% nital etch.

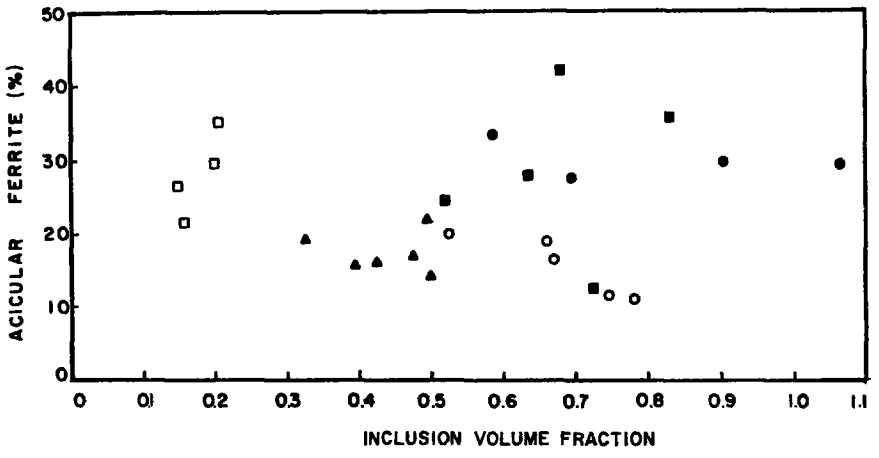

Figure 9 Correlation between the amount of acicular ferrite and the inclusion volume fraction for all the welds produced in this work. (●) 40% SiO_2–FeO–MnO, (■) 40% SiO_2–CaF_2–MnO, (○) 40% SiO_2–CaO–CaF_2, (▲) 30% SiO_2–CaO–CaF_2, (□) 20% SiO_2–CaO–CaF_2.

amounts of acicular ferrite than those welds from the SiO_2–CaO–CaF_2 fluxes, in spite of the fact that the later welds have lower oxygen contents, (Figs 2 and 3), and within a so called "optimum oxygen range" [4, 13, 15]. The weld inclusion volume fraction range for both systems is similar, as shown in Fig. 4, however a close observation of their chemistries show larger manganese levels for the SiO_2–MnO–CaF_2 welds than for the SiO_2–CaO–CaF_2 welds, Table III. A number of investigations [34–36] indicate that manganese affects the weld metal microstructure by shifting the austenite decomposition transformation to larger times increasing the proportion of acicular ferrite. Fig. 11 shows two representative microstructures of the welds in Fig. 10, samples J10 and J11.

The inclusion morphology was difficult to correlate with the weld microstructure due to the difference in the weld composition, particularly in the manganese content. The inclusion size has been referred to as a critical factor in the weld metal transformation. A given size distribution could pin the austenite grain boundary [4, 17] refining the grain and thus increasing the areas favourable for nucleation of high temperature ferrite. However, support has been added to the hypothesis that the inclusions themselves can nucleate ferrite intergranularly or intragranularly [17, 37, 38]. In the present investigation, the reduction of the inclusion size was accompanied by an increase of grain boundary ferrite and reduction of the acicular ferrite. Fig. 5 shows the refinement of the inclusions in welds produced with SiO_2–MnO–CaF_2 fluxes and the corresponding decrease of the acicular ferrite level is shown in Fig. 10. It may be possible that the cooling rates experienced by the welds are too slow and thus fail to activate the fine inclusions as nucleation sites for the ferrite transformation. However the increase of the grain boundary ferrite is an evidence of the pinning action of these inclusions.

Quenching of a hot weld metal sample, J7Q, resulted in a microstructure consisting primarily of acicular ferrite with proeutectoid veining grain boundary ferrite and patches of blocky ferrite (intergranular and intragranular). Fig. 12 shows the microstructure of weld sample J7 that has been air cooled and water

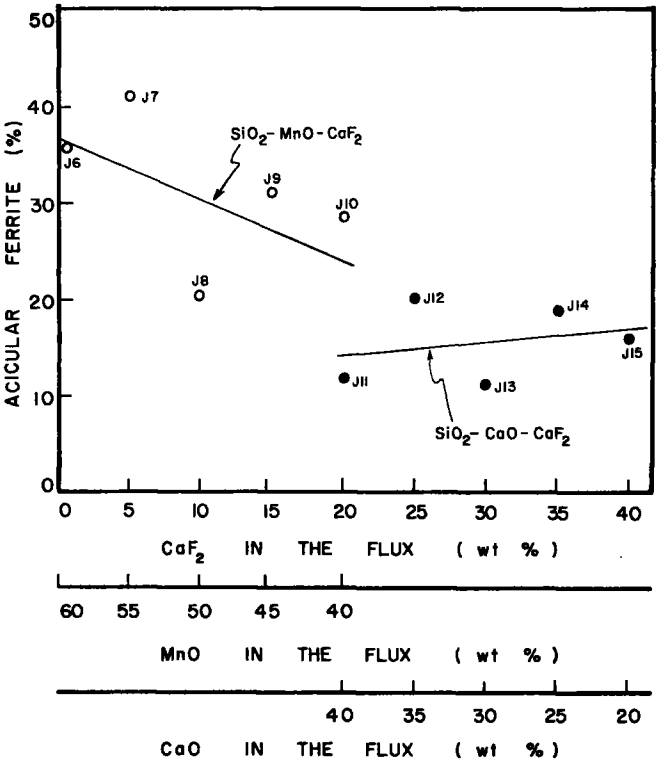

Figure 10 Proportions of acicular ferrite for welds produced with the SiO_2–MnO–CaF_2 and SiO_2–CaO–CaF_2 flux systems. SiO_2 = 40% (constant).

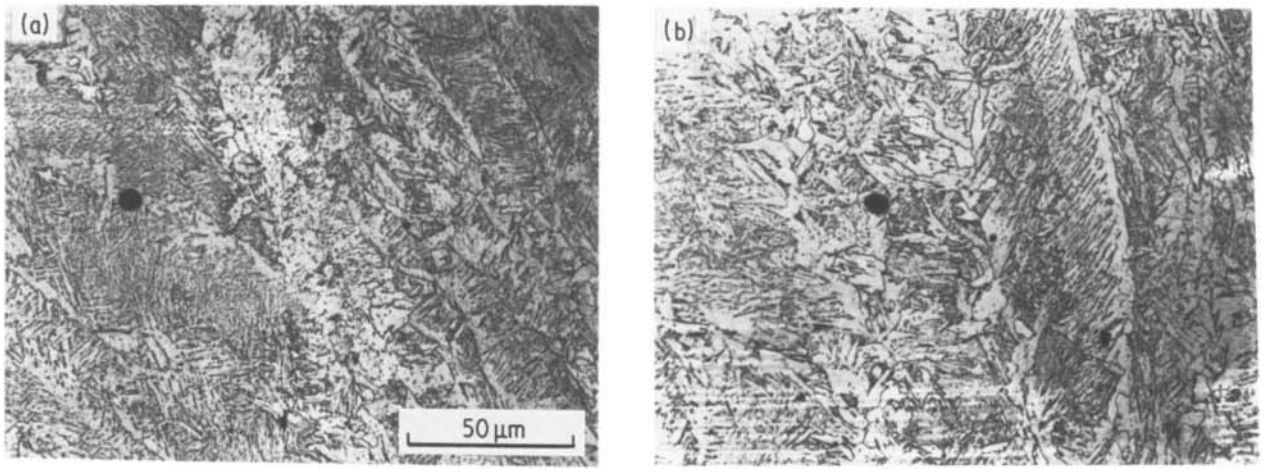

Figure 11 Weld microstructures corresponding to: (a) $40SiO_2-40MnO-20CaF_2$ flux, and (b) $40SiO_2-40CaO-20CaF_2$ flux. 2% nital etch.

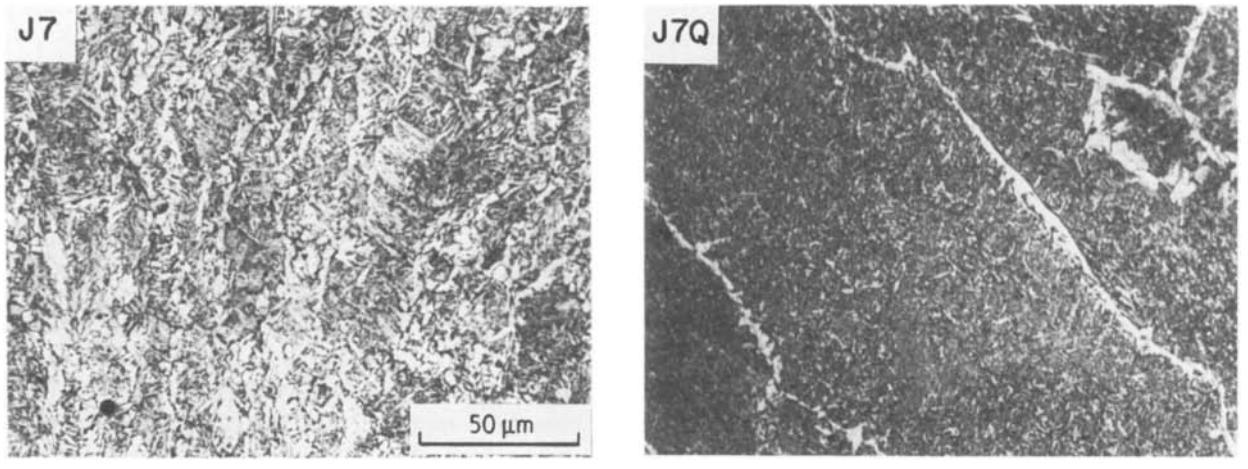

Figure 12 Weld microstructures produced with the $40SiO_2-55MnO-5CaF_2$ flux. J7: air cooled after welding, J7Q: water quenched after welding. 2% nital etch.

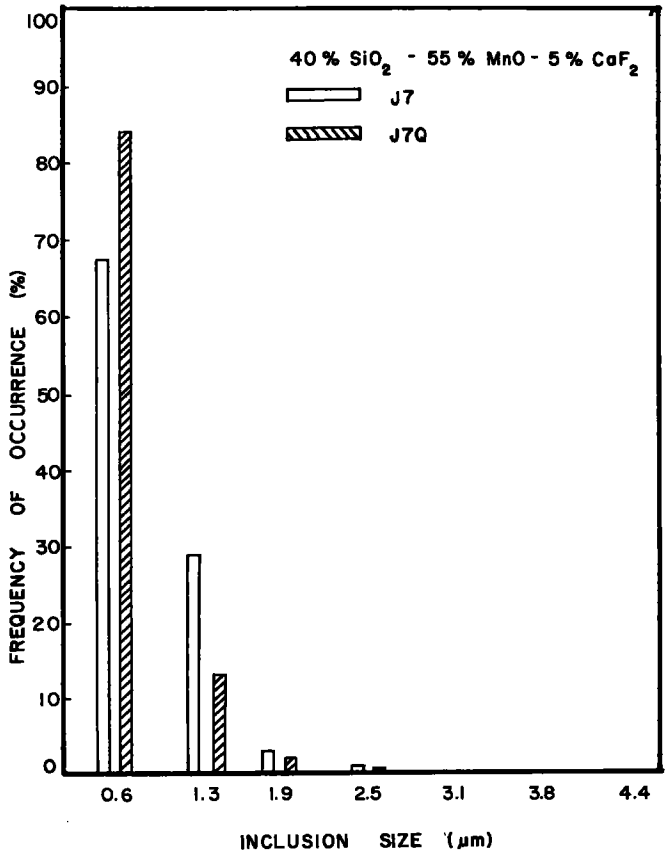

Figure 13 Histogram comparing the inclusion size distribution between samples J7 and J7Q.

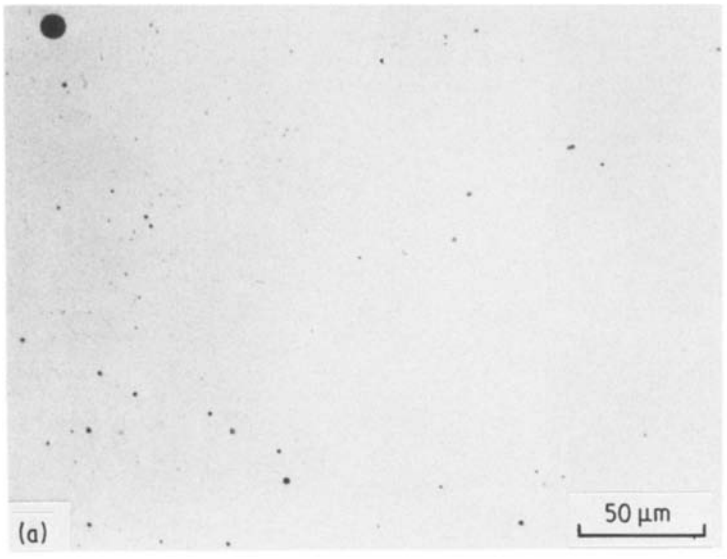

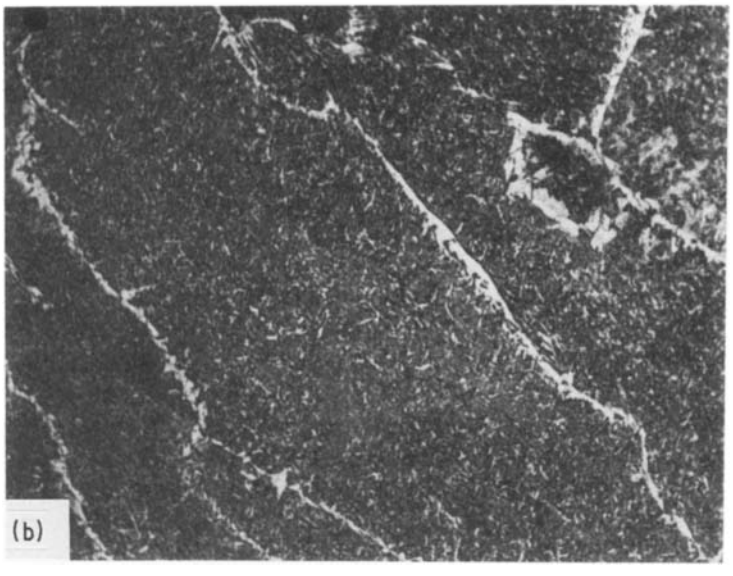

Figure 14 Photomicrographs of weld specimen J7Q showing: (a) inclusion distribution, and (b) corresponding microstructure in the same location. 2% nital etch.

quenched (J7Q). The coarser grains observed in weld sample J7Q, imply reduced pinning activity by the inclusions and their participation as active nucleation sites because of the increase in the amount acicular ferrite. The inclusion count on the J7Q weld sample reveals a decrease in the inclusion volume fraction as well as a refinement of the inclusions compared to sample J7, Fig. 13. The distribution of these inclusions and their role on the ferrite formation was analysed by observing a specific region of sample J7Q in the as-polished and etched conditions, Fig. 14. It was observed that several of these inclusions delineated the proeutectoid grain boundary ferrite. Inclusions of size 1 μm and larger, appear not only to pin the grain boundaries, but they also become nucleation sites for the proeutectoid blocky ferrite. This blocky ferrite is also found intragranularly as shown in Fig. 15. Inclusion of sizes smaller than 0.6 μm, about 0.3 μm, located at the grain boundaries are primarily effective in pinning the grain boundary. Fig. 16 shows inclusions pinning the grain boundary (Fig. 16a) and as nucleants of intergranular blocky ferrite (Fig. 16b). Inclusions about 0.6 μm and smaller located intragranularly can be associated with the acicular ferrite, as shown in Fig. 17.

The chemistry of the inclusions was examined in most of the welds. Manganese, aluminium and titanium were the primary elements present. The inclusions about the acicular ferrite and proeutectoid grain boundary were inspected and it was found that larger proportions of manganese, titanium, aluminium and silicon were present in the inclusions within the acicular ferrite, as seen in Figs 18 and 19. The chemistry of the area adjacent to the inclusions was the same as that of the inclusions. The difference in the magnitude of the peaks implies a higher hardenability in the case of inclusions associated with the acicular ferrite.

Conclusions

The results of this investigation led to the following conclusions:

1. The oxygen content and the inclusion volume fraction of the welds are reduced as the SiO_2 content of the fluxes is reduced and the amount of stable oxide constituents is increased.

2. The inclusion morphology is primarily a function of the oxide constituents of the fluxes and is not directly affected by the basicity of the flux.

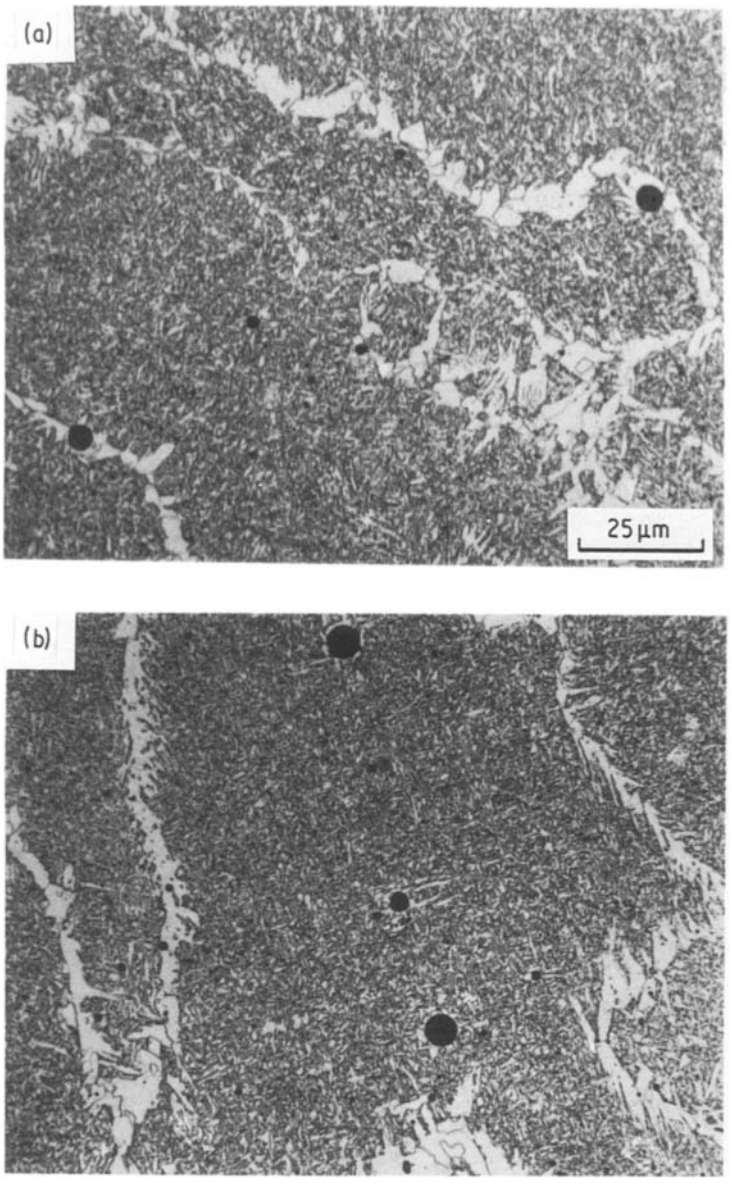

Figure 15 Weld microstructures showing the location of large inclusions: (a) intergranularly at the proeutectoid grain boundary ferrite, and (b) intragranularly with blocky ferrite. 2% nital etch.

3. The size of the non-metallic inclusion determine the extent of their involvement in the weld metal phase transformation. For the cooling rates experienced by these welds inclusions 0.6 μm and smaller are present within the fine acicular ferrite. Large inclusions (1 μm and greater) appear to pin the grain boundary but they also become the nucleation sites for blocky ferrite. The very fine inclusions (less than about 0.3 μm) appear to only pin the grain boundaries.

4. The hardenability and cooling rate are factors that also influence the austenite to ferrite transformation in the weld metal, along with the inclusions.

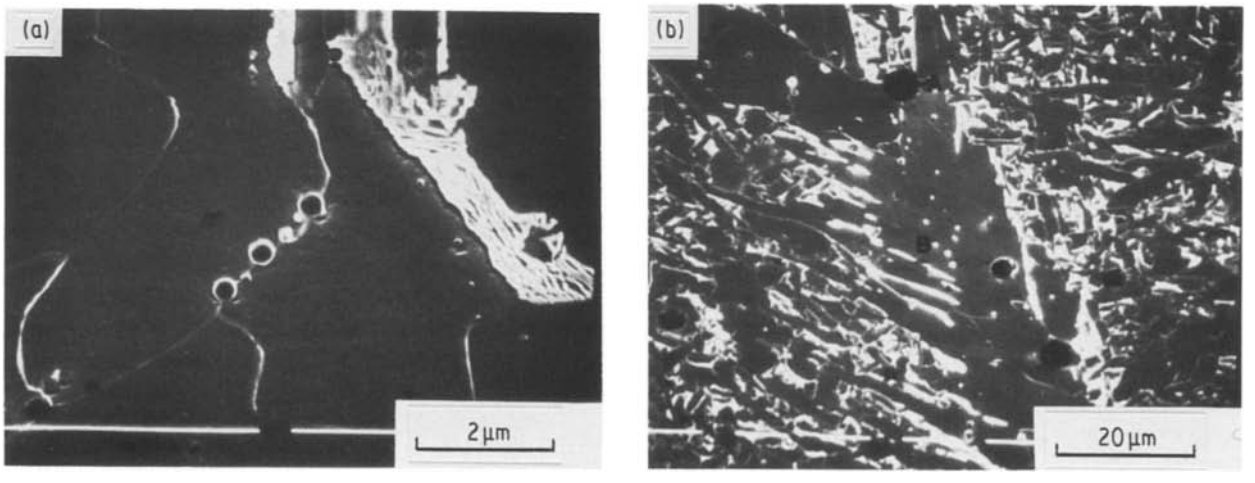

Figure 16 Scanning electron micrographs for a weld specimen produced with the $40SiO_2-55MnO-5CaF_2$ flux. (a) Inclusions pinning the grain boundary, and (b) inclusions within the proeutectoid grain boundary.

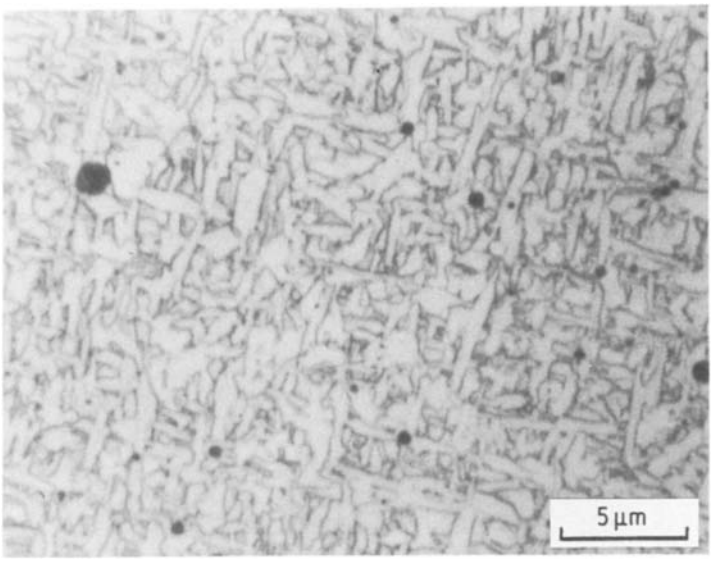

Figure 17 Weld metal acicular ferrite with small inclusions located within the ferrite plates. 2% nital etch.

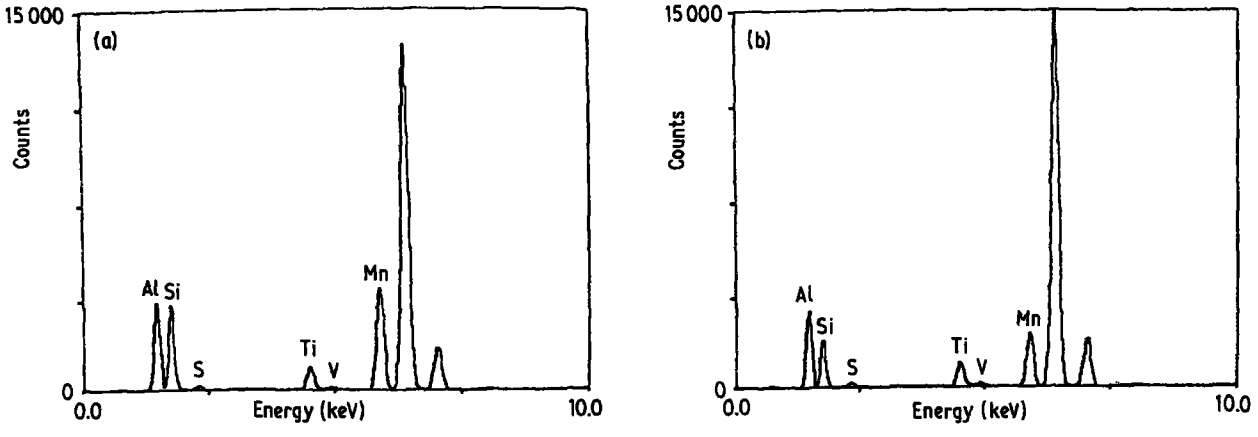

Figure 18 EDS X-ray spectra for inclusions located at: (a) the acicular ferrite, and (b) the proeutectoid grain boundary ferrite. The weld specimen was produced with the $40SiO_2-40CaF_2-20CaO$ flux.

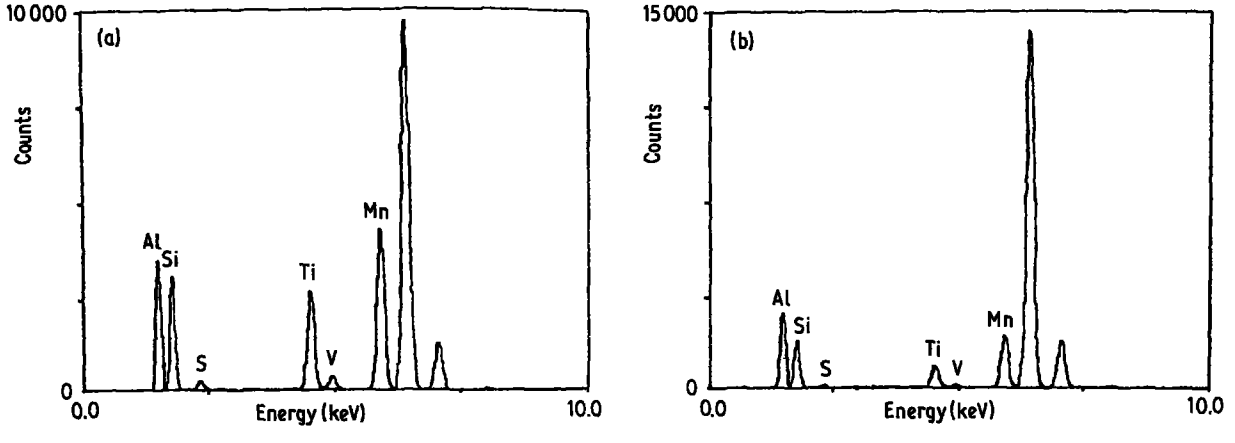

Figure 19 EDS X-Ray spectra for inclusions in the weld metal. (a) at the acicular ferrite, and (b) at the proeutectoid grain boundary ferrite. The weld specimen was produced with the $40SiO_2-55MnO-5CaF_2$ flux.

References

1. R. A. KUBLI and W. W. SHARAV, *Welding J.* **40** (1961) 497-s.
2. K. MASUBUSHI, R. E. MONROE and D. C. MARTIN, WRC Bulletin January 1966, 111.
3. Y. ITO and M. NAKANISH, *Sumitomo Search* **15** (1976) 42.
4. R. C. COCHRANE and P. R. KIRKWOOD, "in Conference Proceedings of the Trends in Steel and Consumables for Welding", London Paper 35. (The Welding Institute, London, 1978) p. 103.
5. B. R. KEVILLE and R. C. COCHRANE, "Factors Controlling the Microstructure and Toughness of Submerged-Arc-Welding", Proceedings of the 30th Annual Conference of the Australian Welding Institute, October (1982) p. 263.
6. R. KOHNO, T. TAKAMI, N. MORI and K. NAGANO, *Welding J.* **61** (1982) 373-s.
7. T. W. EAGER, *ibid.* **57** (1978) 76-s.
8. S. S. TULIANI, T. BONISZEWSKI and N. F. EATON, *Welding and Metal Fabrication* **37** (1969) 327.
9. J. J. LEWIS, G. E. FAULKNER and P. J. RIEPPEL, *Welding J.* **40** (1961) 337-s.

10. J. G. GARLAND and P. R. KIRKWOOD, *Welding and Metal Fabrication* **44** (1976) 217.
11. L. G. TAYLOR and R. A. FARRAR, *ibid.* **43** (1975) 305.
12. H. TERASHIMA and J. TSUBOI, *Metal Construction* **14** (1982) 472.
13. L. DEVILLERS, B. MARANDET, D. KAPLAN, A. RIBES and P. V. RIBOUD, in Proceedings of ECF Conference on Fracture toughness and Microstructures, of submerged arc weld metal, Leoben, Austria, September 1982.
14. D. J. ABSON and R. E. DOLBY. *The Welding Institute Research Bulletin* **21** April (1980) 100.
15. D. J. ABSON, R. E. DOLBY and P. H. M. HART, in Proceedings of International Conference on Trends in Steels and Consumables for Welding, London, November, 1978 (The Welding Institute, 1978) p. 75.
16. D. J. ABSON, "The Role of Inclusions in Controlling Weld Metal Microstructures in C-Mn Steels", The Welding Institute Research Report 69/1978/M.
17. P. L. HARRISON and R. A. FARRAR, *J. Mater. Sci* **16** (1981) 2218.
18. M. E. IAGGESSE, A. R. BHATLI, D. N. HAWKINS and J. A. WHITEMAN, in Proceedings of the International Conference on The Effects of Residual, Impurity and Micro-alloying Elements on Weldability and Weld Properties", London, November 1983, Paper 15 (The Welding Institute, 1983).
19. B. L. BRAMFITT, *Met. Trans.* **1A** (1970) 1987.
20. I. WATANABE and T. KOJIMA, *J. Welding Soc. Part I* **49** (1980) 772.
21. *Idem, ibid. Part II* **50** (1981) 702.
22. N. MORI, H. HIROYUKI, S. OKITA and M. WAKABAYASHI, Mechanism of notch toughness improvements in Ti–B bearing weld metals. IIW Doc. IX-1196-81.
23. A. R. BHATTI, M. E. SAGGESE, D. N. HAWKINS, J. A. WHITEMAN, and M. S. GOLDING, *Welding J.* **63** (1984) 224-s.
24. D. BROOKSBANK and K. W. ANDREWS, *J. Iron and Steel Institute* **210** (1972) 246.
25. R. KIESSLING, "Non-Metallic Inclusions in Steel", Parts I–IV, (The Metal Society, London, 1978).
26. R. J. PARGETER, "Investigation of submerged arc weld metal inclusions", WIRR 151/1981 (1981).
27. L. DEVILLERS, D. KAPLAN, B. MARANDET, A. RIBES, and P. V. RIBOUD, in Proceedings of the International Conference on The Effects of Residual, Impurity and Micro-alloying Elements on Weldability and Weld Properties". Paper I (The Welding Institute, London, 1983).
28. M. FARRANTE and R. A. FARRAR, *J. Mater. Sci.* **17** (1982) 3293.
29. B. AHLBLOM, "Oxygen and It's Role in Determining Weld Metal Microstructure and Toughness – A State of the Art Review", IIW Doc IX-1322-84 (1984).
30. B. R. KEVILLE, *Welding J.* **62** (1983) 253-s.
31. F. D. RICHARDSON, "The Physical Chemistry of Melts in Metallurgy", (Academic Press, London, 1974) pp. 78–115.
32. C. BONNET, *Soudage et Techniques Connexes* **34** (1980) 209.
33. P. L. HARRISON, M. N. WATSON and R. A. FARRAR, *Weld Met. Fabrication* **49** (1981) 161.
34. C. L. CHOI and D. C. HILL, *Welding J.* **57** (1978) 232s.
35. R. A. FARRAR and M. N. WATSON, "Effect of Oxygen and Manganese on Submerged Arc Weld Metal Microstructure". Metal Construction, **11** (1979) 285.
36. G. M. EVANS, *Welding J.* **59** (1980) 67s.
37. M. FARRANTE and R. A. FARRAR, *J. Mater. Sci.* **17** (1982) 3293.
38. R. A. RICKS, P. R. HOWELL and G. S. BARRITE, *J. Mater. Sci.* **17** (1982) 732.

Received 6 January
and accepted 30 June 1986